Journal of Materials Chemistry A

PAPER

View Article Online
View Journal | View Issue

Cite this: J. Mater. Chem. A, 2019, 7, 14328

Shape-tailorable high-energy asymmetric micro-supercapacitors based on plasma reduced and nitrogen-doped graphene oxide and MoO_2 nanoparticles†

Liangzhu Zhang, ‡[a] Zhiqiang Chen,‡[a] Shuanghao Zheng,[bc] Si Qin, [a] Jiemin Wang,[a] Cheng Chen,[a] Dan Liu,*[a] Lifeng Wang,[a] Guoliang Yang,[a] Yuyu Su,[a] Zhong-Shuai Wu, *[b] Xinhe Bao, [b] Joselito Razal [a] and Weiwei Lei *[a]

Asymmetric micro-supercapacitors (AMSCs) are considered to be highly competitive miniaturized energy-storage units for wearable and portable electronics. However, the energy density, voltage output and fabrication technology for AMSCs remain challenges for practical applications. Herein, we adopt plasma reduced and nitrogen-doped graphene oxide with a high nitrogen content of 8.05% and ultra-fine MoO_2 nanoparticles with a diameter of 5–10 nm as electrode materials for high-energy flexible all-solid-state AMSCs. The AMSCs based on plasma reduced and nitrogen-doped graphene oxide (PNG) and plasma reduced and nitrogen-doped graphene oxide–MoO_2 composite films (PNG–MoO_2) can be integrated on diverse substrates (*e.g.*, cloth, glass, leaves, and polyethylene terephthalate (PET) films) and tailored into microelectrodes with various planar geometries by accurate laser cutting. The resulting PNG//PNG–MoO_2-AMSCs exhibit a high working voltage of 1.4 V, a significant areal capacitance of 33.6 mF cm^{-2} and an outstanding volumetric capacitance of 152.9 F cm^{-3} at 5 mV s^{-1}, and offer an exceptionally high energy density of 38.1 mW h cm^{-3}, outperforming most reported AMSCs. Furthermore, the microdevices demonstrate electrochemical performance with excellent stability under various bending conditions up to 180° and without obvious capacitance degradation even after being bent at 60° for 1000 times. Furthermore, PNG//PNG–MoO_2-AMSCs displayed exceptional serial and parallel integration to boost the output of voltage and capacitance. This work demonstrates the great potential of such AMSCs for practical application in miniaturized, wearable, and flexible electronics.

Received 5th April 2019
Accepted 17th May 2019

DOI: 10.1039/c9ta03620b

rsc.li/materials-a

Introduction

The rapid development in the field of miniaturization of portable and wearable electronic devices has increased the demand for miniaturized energy storage and micro-power supply.[1–5] Compared to commercially available Li thin-film or microscale batteries, planar micro-supercapacitors (MSCs) as a novel type of microscale energy storage device have attracted tremendous attention due to their ultra-long lifetime and impressive power density, and being separator free and free of lithium-related safety issues.[6,7] In addition, MSCs with an in-plane configuration not only endow the device with high flexibility but can also be integrated efficiently on-chips and in-package within miniaturized electronics.[8–11] However, most of the reported MSCs cannot meet the requirement of high voltage output, volumetric capacitance and energy density without sacrificing their power density and lifetime, which limited their practical applications in flexible and portable electronics.

Recently, graphene has been considered an ideal two dimensional material for MSCs to maximize the advantages of the planar device configuration and energy storage due to its high surface area, outstanding electrical conductivity and large specific capacitance. For example, MSCs based on reduced graphene oxide, graphene quantum dots and graphene composites have demonstrated the merits of robust flexibility, scalability, ultra-long cyclability and high power density.[12–20] To

[a]Institute for Frontier Materials, Deakin University, Waurn Ponds Campus, Locked Bag 20000, Victoria 3220, Australia. E-mail: dan.liu@deakin.edu.au; weiwei.lei@deakin.edu.au

[b]Dalian National Laboratory for Clean Energy, Dalian Institute of Chemical Physics, Chinese Academy of Sciences, 457 Zhongshan Road, Dalian 116023, China. E-mail: wuzs@dicp.ac.cn

[c]University of Chinese Academy of Sciences, 19 A Yuquan Rd, Shijingshan District, Beijing, 100049, China

† Electronic supplementary information (ESI) available. See DOI: 10.1039/c9ta03620b

‡ Liangzhu Zhang and Zhiqiang Chen contributed equally to this work.

further boost the energy density (E) of graphene based MSCs, it is efficient to implement high specific capacitance (C) electrode materials with different working potentials in an asymmetric configuration to increase the output voltage (V), namely graphene based AMSCs, in terms of $E = 0.5CV^2$.[21–23] Nitrogen doped graphene (NG) has larger specific capacitance compared with pristine graphene due to additional pseudocapacitive effects, which is an ideal film material for negative electrodes.[24–28] In addition, the fabrication of a heterogeneous film incorporated with pseudocapacitive metal oxides (RuO_2, MnO_2, Fe_2O_3, and MoO_2) and graphene as the positive electrode material is another efficient strategy for providing synergistic benefits in terms of electrochemical and mechanical performance.[29–33] Until now, most NG or graphene heterogeneous film electrodes reported are based on *in situ* CVD,[34] and post-reduction treatment of graphene oxide (GO) films by thermal, solvothermal, laser and hydrothermal methods.[35–37] However, most of these methods usually require multi-step procedures, toxic chemical substances, high temperature and annealing processes, which lead to poor compatibility with various substrates and subsequent device fabrication techniques for scalable and integrated applications.[14] Furthermore, mask-assisted vacuum filtration, inkjet printing, electrochemical deposition, and micro-electro-mechanical system (MEMS) fabrication have been applied to fabricate asymmetric micro-supercapacitors, and these are still not efficient and economic enough to implement the assembly and integration on various substrates as well as scalable production.[38–43] Therefore, a feasible and practical strategy that features nitrogen-doped reduced graphene oxide which enables the assembly of composite materials with an optimal ratio of pseudocapacitive species for flexible patterning and large area film electrodes for AMSCs is still in high demand for ready integration into miniaturized electronic devices.

In this work, we developed flexible high-energy all-solid-state AMSCs with diverse planar micropatterns based on plasma reduced and nitrogen-doped graphene oxide and ultra-fine MoO_2 nanoparticles. The AMSCs consist of a PNG film as the negative electrode and a PNG–MoO_2 film as the positive electrode, which was denoted as PNG//PNG–MoO_2-AMSCs. This plasma technique, combined with laser cutting, brings great advantages of applicable scalability, high efficiency, low cost, environmental benignity, and versatile post-tailored geometries and size, which can be readily integrated and is compatible with miniaturized electronic device manufacturing. In addition, the assembled flexible AMSCs can be transferred onto various substrates (*e.g.* glass, leaves, and PET). Notably, the flexible PNG//PNG–MoO_2-AMSCs delivered an outstanding areal capacitance of 33.6 mF cm^{-2}, a volumetric capacitance of 152.9 F cm^{-3}, and a remarkable energy density of 38.1 mW h cm^{-3}. Moreover, the PNG//PNG–MoO_2-AMSCs demonstrated excellent cyclability with 88% capacitance retention after 10 000 cycles as well as exceptional mechanical flexibility with ~97.2% capacitance retention after repeatedly bending to 60° for 1000 times. We believe that our demonstration of PNG//PNG–MoO_2-AMSCs will offer opportunities to power various miniaturized wearable electronic devices.

Experimental section

Materials synthesis

All chemicals are purchased from Sigma Aldrich without further purification. GO solution with a concentration of 5 mg mL^{-1} was synthesized by Hummers' method.[44] A MoO_2 solution with a concentration of 3.4 mg mL^{-1} was prepared *via* a hydrothermal method.[45] In detail, 0.3 g commercial MoO_3 powder (Sigma Aldrich, metal basis, 99%), 10 mL absolute ethylene glycol (Sigma Aldrich, analytical grade, 99%) and 10 mL DI water were stirred for 30 minutes. The mixture was transferred into a 100 mL Teflon-lined stainless steel autoclave. The autoclave was sealed and put into an oven at 120 °C for 6 h. After the autoclave cooled down, the dark solution was centrifuged and washed several times at 3500 rpm. Then the upper MoO_2 solution was collected by centrifuging at 7000 rpm for 30 min. The final MoO_2 colloidal solution was obtained with a concentration of 3.4 mg mL^{-1}.

Fabrication of RGO-MSCs and PNG-MSCs

To fabricate a thin GO film for MSCs, the layer-by-layer deposition method was used, as we reported recently.[19,46] 10 mg GO solution was added into 50 mL DI water by sonication for 10 min, and then the GO film was obtained by directly vacuum filtering the solution onto cellulose paper. The RGO film was prepared by heat reducing the GO film in an oven at 200 °C for 24 hours. The PNG film was obtained by treatment with N_2/H_2 (15 vol%) plasma with a 200 W power for 1 hour in a homemade plasma system. The gold layer was sputtered on both of the PNG and RGO films with a rate of 0.5 nm s^{-1} at a chamber pressure of 9×10^{-3} mbar. The microelectrodes were prepared by laser cutting of the corresponding RGO and PNG films. Finally, the patterned microelectrodes were assembled on PET with dual adhesive tape and a polymer gel electrolyte PVA–LiCl was carefully drop-casted. RGO-MSCs are based on RGO microelectrodes. PNG-MSCs are based on PNG microelectrodes.

Fabrication of RGO//RGO–MoO_2-AMSCs and PNG//PNG–MoO_2-AMSCs

To prepare GO–MoO_2 films, 10 mg GO sheets and 1.1 mg MoO_2 nanoparticles (the mass ratio of GO–MoO_2 is 9 : 1) were added into 50 mL DI water by sonication for 10 min, and then the GO–MoO_2 films were obtained by directly vacuum filtering the solution onto cellulose paper. Subsequently, PNG–MoO_2 films were prepared by using a homemade plasma system using a N_2/H_2 (15 vol%) gas with a 200 W power for 1 hour. RGO–MoO_2 films were obtained in an oven at 200 °C for 24 hours. A 40 nm gold layer was sputtered on both of PNG and PNG–MoO_2 films with a rate of 0.5 nm s^{-1} at a chamber pressure of 9×10^{-3} mbar. The PNG, PNG–MoO_2, RGO and RGO–MoO_2 microelectrodes were prepared by laser cutting the films (Dobot Robot Shenzhen Yuejiang Technology Co., Ltd.). Finally, the patterned microelectrodes were assembled on PET using dual adhesive tape and a polymer gel electrolyte of PVA–LiCl was carefully drop-casted. The PNG//PNG–MoO_2-AMSCs are based on PNG

and PNG–MoO_2 microelectrodes. The RGO//RGO–MoO_2-AMSCs are based on RGO and RGO–MoO_2 microelectrodes.

Materials characterization

Materials characterization for the structure and morphology was performed by XRD (PAN analytical X'pert Pro.), FTIR (Bruker Vertex-70), Raman spectroscopy (Renishaw), XPS (Kratos AXIS Nova instrument equipped with a monochromatic Al Kα X-ray source), TGA (Q-500, TA Instruments), SEM (Zeiss Supra 55VP) and Transmission Electron Microscopy (TEM) (JEOL 2100). Sheet resistance was measured by using a conductivity meter with a four point probe head (ST22588-F01, Suzhou Jingge Electronic Co., Ltd.).

Electrochemical measurement

The electrochemical performance of the fabricated devices was measured by CV tests from 5 to 200 mV s^{-1}. The GCD test took measurements at different current densities and electrochemical impendence spectroscopy was performed in the frequency range of 0.1 Hz to 100 kHz with a 5 mV AC amplitude. All the electrochemical measurements were carried out using an electrochemical workstation (reference 600+, Garmy Co., Ltd).

Results and discussion

Fig. 1a schematically illustrates the fabrication procedure of all-solid-state planar PNG//PNG–MoO_2-AMSCs based on PNG and PNG–MoO_2 films. First, a thin film of GO was fabricated onto paper by vacuum filtration of a 50 mL well dispersed GO (10 mg) solution. A GO–MoO_2 film was prepared by the same method using 50 mL mixed solutions of GO sheets (10 mg) and MoO_2 nanoparticles (1.1 mg). TEM images show ultra-fine MoO_2 nanoparticles with a diameter of 5–10 nm (Fig. S1 and S2†). The SEM image of the GO film displays a uniform and flat surface (Fig. S3a and b†), while the GO–MoO_2 film shows a wrinkled and rough surface due to the uniformly dispersed MoO_2 nanoparticles in GO as pinning obstacles which effectively prevent the restacking of GO after reduction (Fig. S3c and d†). The cross-sectional images of PNG and PNG–MoO_2 reveal the compact stacking of PNG sheets and PNG–MoO_2 composites with a uniform thickness of ~2.2 μm and 2.3 μm, respectively (Fig. S3e and f†). In addition, TGA indicates that there is 13 wt% MoO_2 in the composite (Fig. S4†).

The simultaneous reduction and N-doping of GO and GO–MoO_2 films were realized by plasma-assisted treatment with N_2/H_2 (15 vol%) gas for 1 h. After plasma treatment, it can be clearly seen that the colour of the GO film changed from yellow brown to dark black, as shown in Fig. S5,† indicating the successful reduction of GO. The SEM image of the PNG–MoO_2 film shows a surface morphology similar to that of the GO–MoO_2 film (Fig. 1b, c and S3c†). The PNG and PNG–MoO_2 films exhibit sheet resistances of 2.3×10^4 Ω sq^{-1} and 2.5×10^4 Ω sq^{-1}, respectively, tested by using the four-point probe method before gold coating. The sheet resistances of the RGO and RGO–MoO_2 films are 4.6×10^6 Ω sq^{-1} and 5.1×10^6 Ω sq^{-1}. The sheet resistance of plasma reduced graphene oxide is much lower than that of the reduced graphene oxide by thermal reduction treatment at 150 °C (2.14×10^6 Ω sq^{-1}),[47] suggesting its superior electrical conductivity and a highly effective plasma-assisted reduction at a low temperature (~50 °C). The corresponding elemental mapping images in Fig. 1d–g show the highly homogeneous C, N, Mo, and O elements in the PNG–MoO_2 film, which demonstrates the successful formation of nitrogen-doped reduced graphene oxide. The reduction and nitrogen-doping effects on the GO/GO–MoO_2 film during plasma processes can be confirmed and quantified by XPS. The XPS survey data (Table S1†) show an oxygen content is 28.57 at% in the GO film and 14.03 at% in the PNG film. The O/C atomic ratio is 0.40 for the GO film, which is much larger than 0.18 for the PNG film. Except for C1s and O1s peaks centered at 284.7 eV and 530 eV in GO, an additional N1s feature appears at 400 eV in PNG, accompanied by a dramatic decrease of O1s peak intensity (Fig. S6†). The high-resolution N1s spectrum of PNG can be deconvoluted into three peaks locating at 396.2 eV, 397.9 eV and 402.5 eV, which can be assigned to pyridinic, pyrrolic and graphitic N (Fig. S6c†).[48–51] It has been reported that the graphitic and pyridinic N on the graphene surface can greatly increase the quantum capacitance of nitrogen-doped reduced graphene oxide compared to pristine graphene, which indicates that the as-produced PNG could deliver a larger space charge capacitance.[52] The XPS results additionally reveal that the total nitrogen concentration is as high as 8.05 at% in PNG (Table S1†). After plasma treatment, the D bands and G bands of PNG and PNG–MoO_2 in Raman spectra show a red-shift and the relative intensity ratio between the D and G bands (I_D/I_G) decreases from 0.92 for GO to 0.88 for PNG (Fig. S7†), suggesting that the partially ionised N_2/H_2 gas reacts with the oxygen-functional groups on the surface of GO films, leading to the effective reduction of the GO films and re-established the conjugated graphene network (sp^2 carbon). In addition, the disappearance of O–H bands is accompanied by new C–N peaks which emerged in FTIR spectra (in Fig. S8†) after plasma treatment, which further confirm our XPS and Raman results.

After plasma-assisted reduction, a thin layer of gold was deposited on the PNG and PNG–MoO_2 films as current collectors. Laser cutting was used to precisely cut the films into microelectrode patterns with desirable in-plane geometries. This facile technique can potentially enable the scalable production of planar MSCs in different configurations with desirable sizes and geometries, *e.g.* spiral, parallel strips, and interdigital fingers (Fig. 1h–k). More importantly, compared with conventional MSCs which require a specific substrate due to the brittleness of thin graphene films, the obtained MSCs can be feasibly assembled on one substrate and transferred to different substrates (*e.g.*, cloth, PET, leaves, and glass) with the assistance of dual adhesive tape (Fig. 1l–o), which can largely extend their application to a range of devices with different requirements. Therefore, the combination of plasma and laser cutting techniques offers a simple, scalable and effective method to fabricate planar and flexible AMSCs. Finally, the all-solid-state planar PNG//PNG–MoO_2-AMSCs were obtained by drop casting the PVA/LiCl electrolyte.

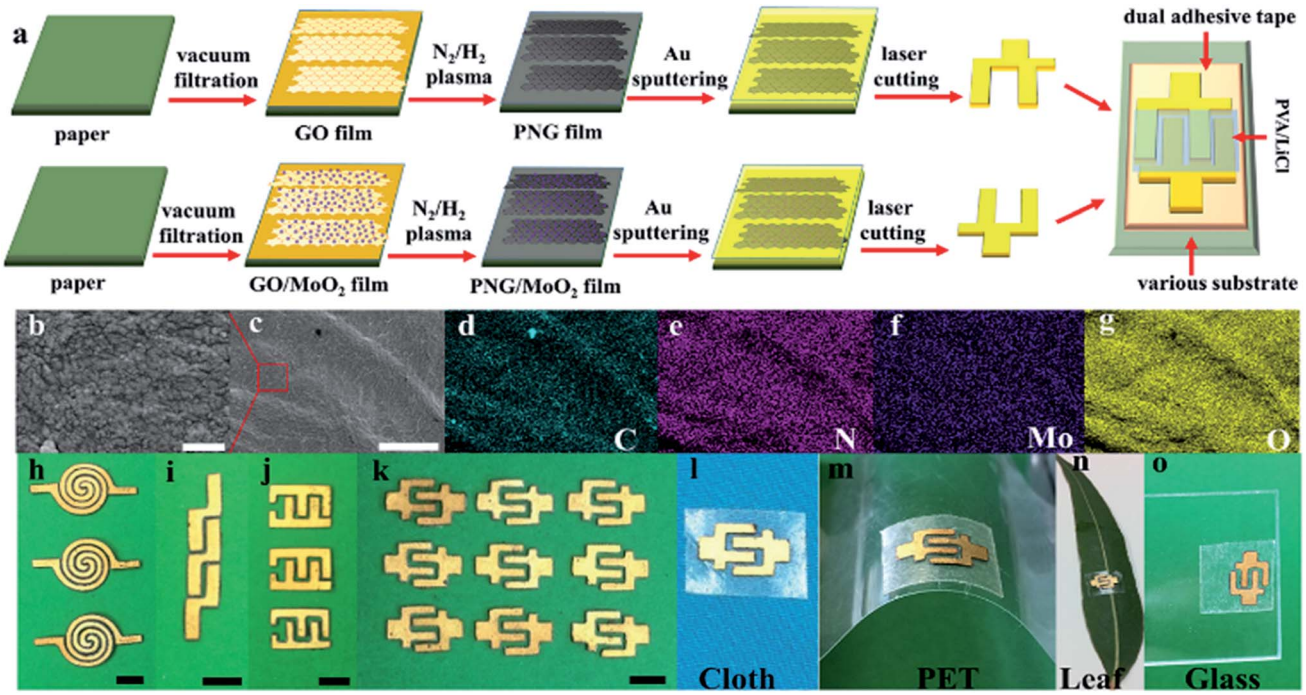

Fig. 1 Fabrication and characterization of flexible in-plane PNG//PNG–MoO_2-AMSCs. (a) Schematic diagram of the fabrication process of PNG//PNG–MoO_2-AMSCs. (b) SEM image of the surface of PNG–MoO_2 at high resolution, and scale bar is 500 nm. (c) SEM image of the surface of the PNG–MoO_2 film at low resolution, with a scale bar of 25 μm. (d–g) Elemental mapping analysis of the PNG–MoO_2 film. Photography of PNG//PNG–MoO_2-AMSCs with various sizes and shapes of (h) spiral, (i) two parallel strips, (j) parallel interdigital fingers, and (k) nine parallel interdigital PNG//PNG–MoO_2-AMSCs assembled on one paper, and a scale bar of 0.5 mm for figures h to k. PNG//PNG–MoO_2-AMSCs transferred onto different substrates: (l) cloth, (m) PET, (n) leaf, and (o) glass.

The nitrogen doping effect on improving the capacitance was ascertained by comparing the electrochemical performance of RGO-MSCs and PNG-MSCs. To be more specific, the positively charged graphitic N is located on the valley and the centre position of the defective graphene lattice. This structure delivers the largest binding energy difference compared with the pure graphene counterpart, which improves the electronic conductivity, electron transfer rate and capacitance. The negatively charged pyridinic N and pyrrolic N could further increase the capacitance *via* enlarging the binding energy at both basal planes and edges.[27] Fig. S9† shows the electrochemical performance results of PNG-MSCs and RGO-MSCs. The rectangle shape of CV curves and the symmetric triangle shape of GCD curves of RGO-MSCs and PNG-MSCs show the typical electrochemical response of electrochemical double layer capacitance (EDLC) materials. An areal capacitance of 37.1 mF cm^{-2} and a volumetric capacitance of 166.9 mF cm^{-3} were obtained for PNG-MSCs at 5 mV s^{-1}, which is four times larger than the areal capacitance of 8.5 mF cm^{-2} and 38.5 mF cm^{-3} for RGO-MSCs (Fig. S9†). The improved capacitance of PNG-MSCs derived from the additional active sites, excellent wettability and enhanced conductivity compared with RGO-MSCs.[53] Therefore, PNG is expected to be a better electrode material to obtain high-performance AMSCs.

Fig. 2a schematically shows the adsorption and intercalation process of PNG//PNG–MoO_2-AMSCs. AMSCs have an in-plane geometry, in which positive and negative electrodes are separated in an interdigital structure. The unique structure increases the ability of the electrolyte ions Cl^- and Li^+ to percolate into the PNG and PNG–MoO_2 layers by full utilization of the electrochemical surface area.[38] To demonstrate the electrochemical performance of PNG//PNG–MoO_2-AMSCs, we first investigated the working potential window by recording the cyclic voltammetry (CV) curves of the PNG film and PNG–MoO_2 film in a typical three-electrode test. It can be seen that the operating potential window of the PNG electrode is found to be from −0.8 to 0 V *vs.* Ag/AgCl and that for the PNG–MoO_2 electrode is from 0 to 0.6 V, as shown in Fig. S11.† The CV and galvanostatic charge and discharge (GCD) curves of planar PNG//PNG–MoO_2-AMSCs (Fig. 2b and c) were recorded at various working voltages at a constant scan rate (5 mV s^{-1}) and current density (0.5 mA cm^{-2}), respectively, which show a uniform electrochemical response, reaching a stable operating voltage of 1.4 V without obvious redox peaks. In addition, the PNG//PNG–MoO_2-AMSCs exhibit a relatively rectangular shaped CV curve even at high scan rate of 100 mV s^{-1}, suggesting fast charge-transfer kinetics and fast ion transport between the layers of PNG, as shown in Fig. 2a and d.[54,55] Moreover, the symmetric triangular shape of the GCD curves at various current densities up to 2 mA cm^{-2} indicates the good reversibility and capacitive properties of such PNG//PNG–MoO_2-AMSCs (Fig. 2e). Notably, the all-solid-state PNG//PNG–MoO_2-AMSCs delivered an outstanding specific areal capacitance of 33.6 mF cm^{-2} and volumetric capacitance of 152.9 F cm^{-3} at

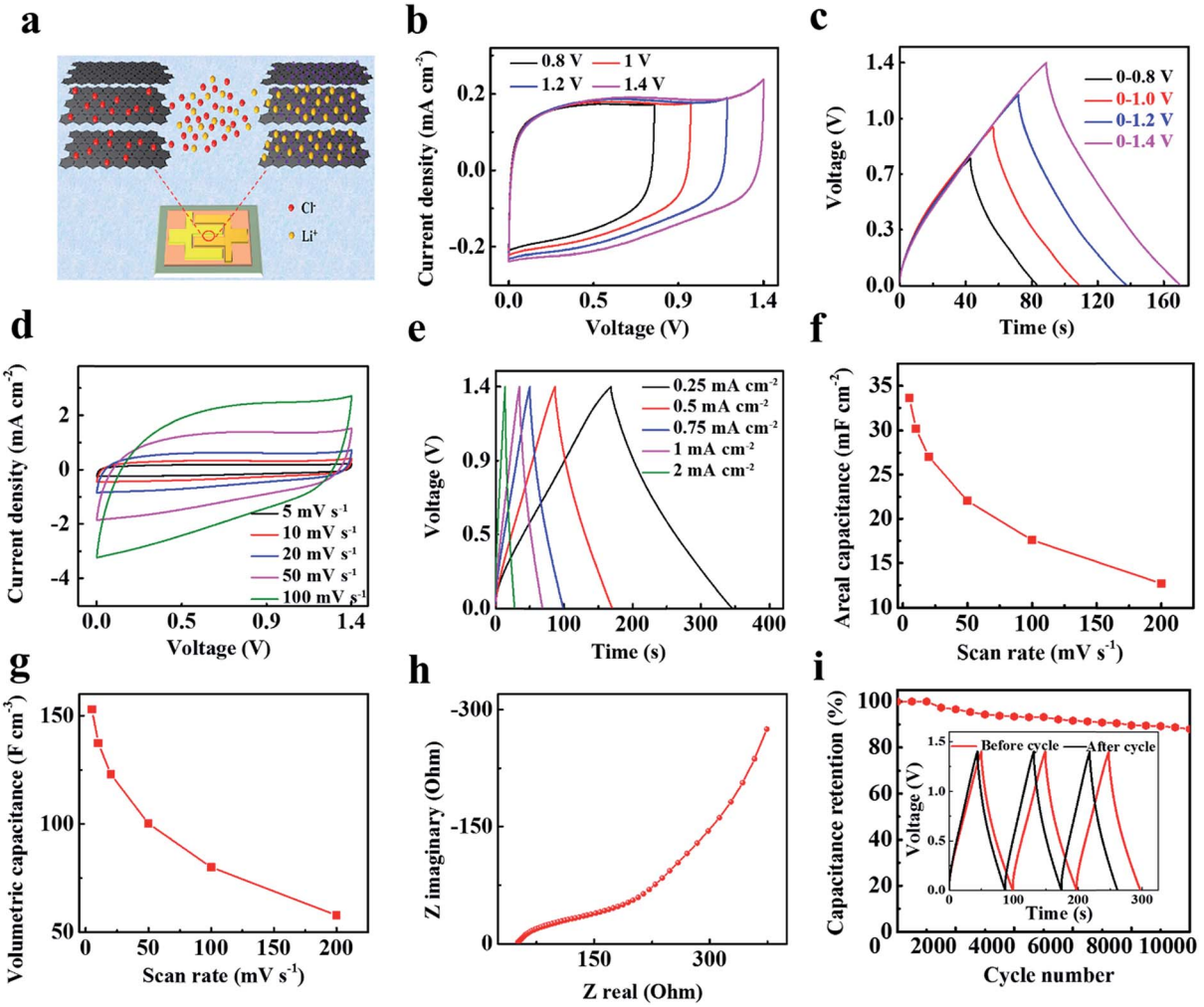

Fig. 2 Electrochemical characterization of in-plane PNG//PNG–MoO_2-AMSCs. (a) Mechanism illustration of PNG//PNG–MoO_2-AMSCs. (b) CV curves of PNG//PNG–MoO_2-AMSCs at different voltages from 0.8 to 1.4 V at a scan rate of 5 mV s^{-1}. (c) GCD curves with different voltages at a current density of 0.5 mA cm^{-2}. (d) CV curves obtained at different scan rates from 5 to 100 mV s^{-1}. (e) GCD curves obtained at various current densities from 0.25 to 2 mA cm^{-2}. (f) Areal capacitance and (g) volumetric capacitance of PNG//PNG–MoO_2-AMSCs. (h) Complex plane plots of PNG//PNG–MoO_2-AMSCs. (i) Cycling stability of PNG//PNG–MoO_2-AMSCs at a current density of 0.75 mA cm^{-2}. Inset shows the GCD curves of PNG//PNG–MoO_2-AMSCs before and after 10 000 cycle.

5 mV s^{-1} (Fig. 2f and g), which is four times larger than the RGO//RGO–MoO_2 areal and volumetric capacitance of 7.9 mF cm^{-2} and 36.2 F cm^{-3}(Fig. S10†). Even at a high scan rate of 200 mV s^{-1}, the areal capacitance and volumetric capacitance were maintained at 12.7 mF cm^{-2} and 57.7 F cm^{-3}, respectively. The Nyquist plot in Fig. 2h shows that the PNG//PNG–MoO_2-AMSCs have an equivalent series resistance (ESR) of ~55 Ω. This ESR is relatively low considering the limited area of the electrodes and the overall small footprint of the device, contributing to excellent rate capability. The specific areal capacitance is much higher than that of most of the latest reported symmetric or asymmetric MSCs (Table S2†), such as photochemically reduced graphene (1.5 mF cm^{-2}),[56] Sulfur-Doped Graphene (0.55 mF cm^{-2}),[57] Fluorine-Doped Graphene (17.4 mF cm^{-2}),[58] LIG–FeOOH//LIG–MnO_2 (21.9 mF cm^{-2}),[59] GP/PANI–G/GP (7.63 mF cm^{-2}),[60] LTO//AG (27.8 mF cm^{-2}),[42] VN//$Co(OH)_2$ (21 mF cm^{-2}),[43] NPG/MnO_2//NPG/PPy (1.27 mF cm^{-2}),[61] and RGO//RGO–MoO_2 (8.7 mF cm^{-2}). More importantly, the as-fabricated PNG//PNG–MoO_2-AMSCs retain 88% of their initial capacitance after 10 000 cycles with a voltage window of 0–1.4 V at a current density of 0.75 mA cm^{-2} (Fig. 2i), manifesting an excellent cycling stability of charge storage. The capacitance fading may result from the partial solubility of MoO_2 due to the residual water in the PVA–LiCl gel electrolyte. The ineffective contact between the active materials and current collector layer after long-term cycling could contribute the degradation as well.[62,63]

To highlight the excellent flexibility of the fabricated AMSCs, we further recorded CV curves of all solid-state PNG//PNG–MoO_2-AMSCs at various bending angles from 0–180° at a scan rate of 50 mV s^{-1} (Fig. 3a and b). Remarkably, all of the CV curves with rectangle patterns almost overlapped and 96.4% of the initial capacitance was maintained even at a high bending angle of 180°, demonstrating the exceptional flexibility and structural integrity of the device. In addition, PNG//PNG–MoO_2-

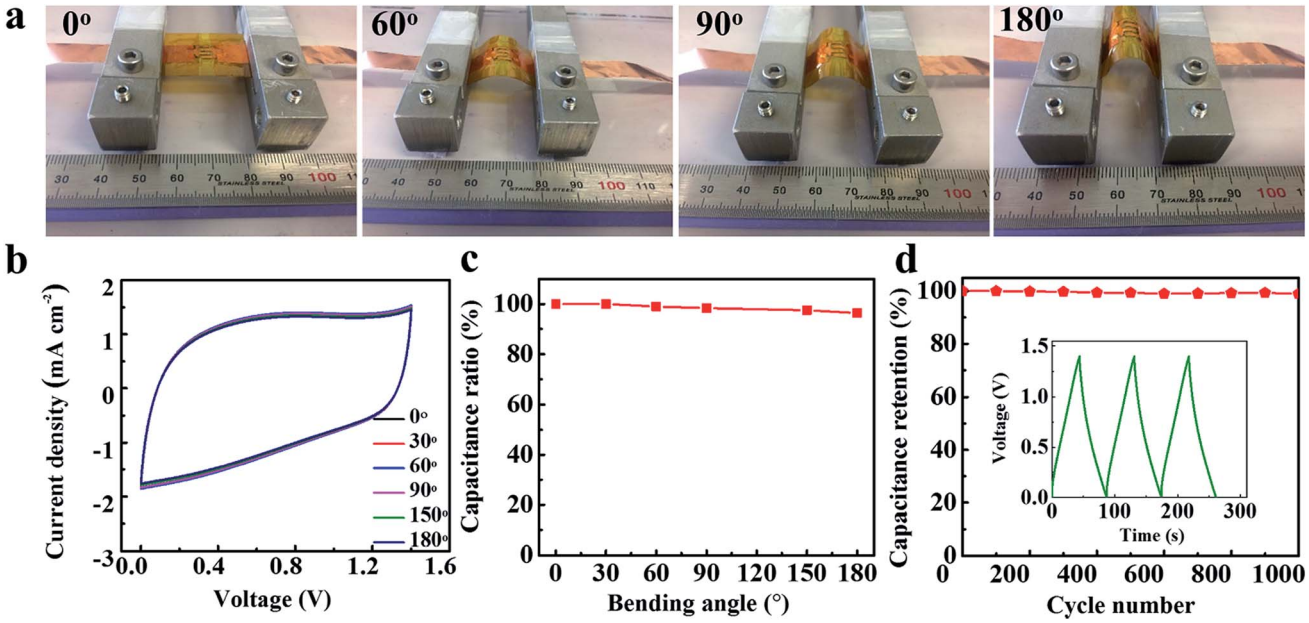

Fig. 3 Flexibility and integration of all-solid-state PNG//PNG–MoO_2-AMSCs. (a) Photographs of PNG//PNG–MoO_2-AMSCs measured under different bending states. (b) CV curves obtained at different bending angles at 50 mV s^{-1}. (c) Capacitance retention as a function of bending angle. (d) Cycling stability of PNG//PNG–MoO_2-AMSCs during repeated bending cycles with a constant bending angle (60°). Inset shows GCD curves recorded at a current density of 0.75 mA cm^{-2}.

AMSCs showed outstanding electrochemical stability and mechanical durability, retaining 97.2% of capacitance after repeatedly bending at 60° for 1000 times. This superior performance makes PNG//PNG–MoO_2-AMSCs a candidate for practical applications in smart garments and flexible electronic devices.

The outstanding electrochemical performance and flexibility of the as-fabricated PNG//PNG–MoO_2-AMSCs should be ascribed to the combined synergistic effects. First, the low sheet resistance and excellent electrical conductivity of both PNG film and PNG–MoO_2 film electrodes after plasma treatment are beneficial to achieve fast charge transfer. The PNG film delivers high capacitance due to the additional pseudocapacitance contributions originated from the nitrogen doping. In addition, nano-sized MoO_2 particles in the PNG–MoO_2 film provide space accommodation to prevent the layer-to-layer stacking during the charge–discharge cycle. The ultrafine structure and good conductivity of MoO_2 particles are beneficial for ion adsorption, intercalation processes and the redox reaction, providing a capacitance enhancement for PNG//PNG–MoO_2-AMSCs.[27,28,64] Secondly, the planar configuration eliminates the need for polymer-based separators required in the sandwich configuration. In particular, the planar configuration allows the ultrafast diffusion of electrolyte ions into (or from) the adjacent graphene based microelectrodes in an extremely short interspace and the full utilization of the highly accessible surface area of PNG and PNG–MoO_2 for charge storage. Furthermore, the cellulose paper with excellent flexibility and strength as a substrate for loading electrode materials is facile to be fabricated into interdigital microelectrodes by laser cutting and integrated onto various substrates, imparting the microdevice with outstanding mechanical flexibility. Last but not least, the usage of a gel electrolyte can not only enhance the contact between the microelectrodes and substrate, but also feature a soft characteristics thus contributing to excellent flexibility and high rate performance.

Superior flexibility, electrochemical stability and high capacitance are performance metrics for practical applications of MSCs. The PNG//PNG–MoO_2-AMSCs can be feasibly assembled and arranged in different configurations, such as in series and/or in parallel (Fig. 4). Four PNG//PNG–MoO_2-AMSCs connected in series can extend the operating voltage window from 1.4 V to 5.6 V, as evidenced by CV and GCD curves at a scan rate of 50 mV s^{-1} and a current density of 0.75 mA cm^{-2}, respectively (Fig. 4a and d). Besides, the parallelly connected PNG//PNG–MoO_2-AMSCs exhibited the stepwise improvement of both current and discharged time, indicative of high performance uniformity of the AMSC units (Fig. 4b and e). Furthermore, different output voltages and discharge times could also be achieved by connecting four PNG//PNG–MoO_2-AMSCs in a fashion of 2 in series and 2 in parallel(Fig. 4c and f). These integrated PNG//PNG–MoO_2-AMSCs were able to light a red light emitting diode (LED) (Fig. 4f and S12†), suggesting the potential of the prepared AMSCs as efficient micro-energy storage units.

High volumetric energy density and power density are critical requirements for the energy storage units of high performance wearable and flexible electronics. The comparison of the as-fabricated PNG//PNG–MoO_2-AMSCs with other commercially available energy storage devices is displayed in the Ragone plot (Fig. 5). Remarkably, the as-prepared PNG//PNG–MoO_2-AMSCs offered an excellent volumetric energy density of 38.7 mW h^{-3} at

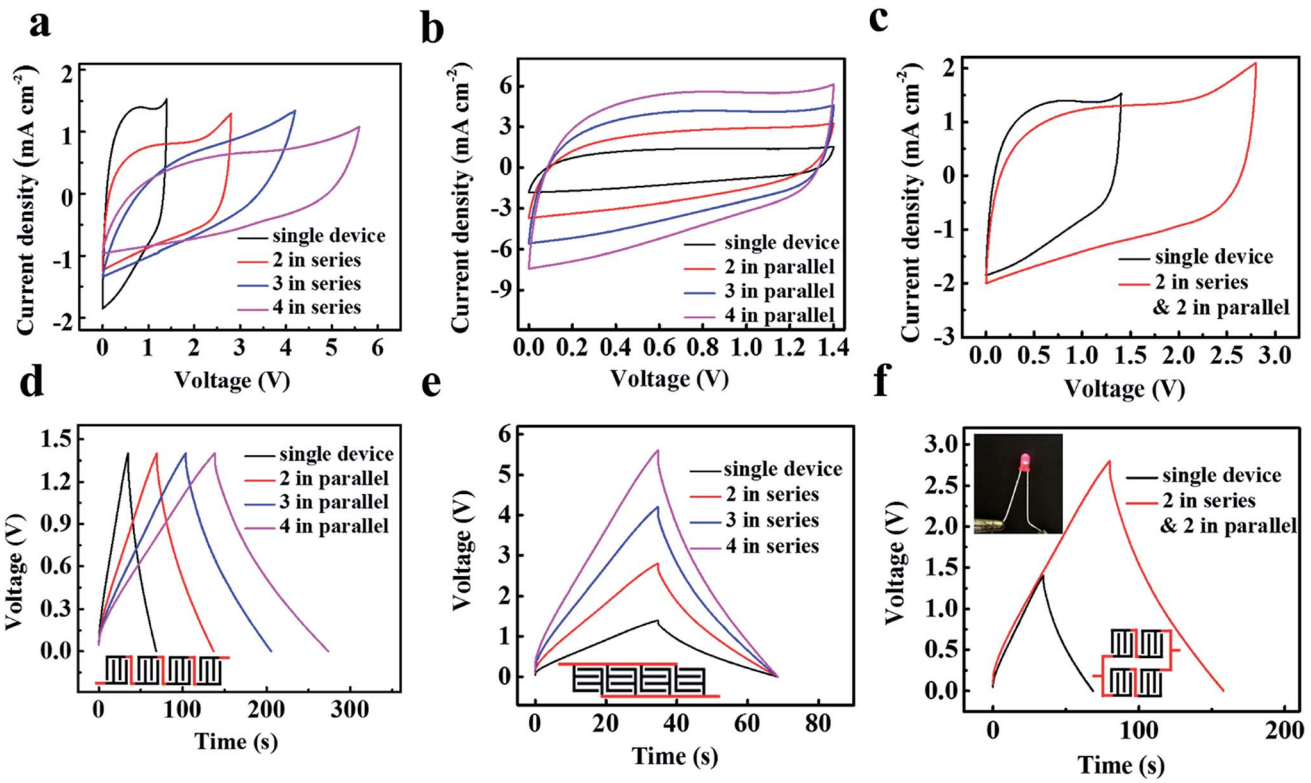

Fig. 4 Integration of PNG//PNG–MoO_2-AMSCs. CV curves of up to four PNG//PNG–MoO_2-AMSCs connected (a) in series, (b) in parallel, and (c) in a combination of 2 series and 2 parallel, tested at 50 mV s^{-1}. GCD curves of four PNG//PNG–MoO_2-AMSCs connected (d) in series, (e) in parallel, and (f) in a combination of 2 series and 2 parallel, obtained at a current density of 0.75 mA cm^{-2} (inset: a red LED was powered by two serially connected devices).

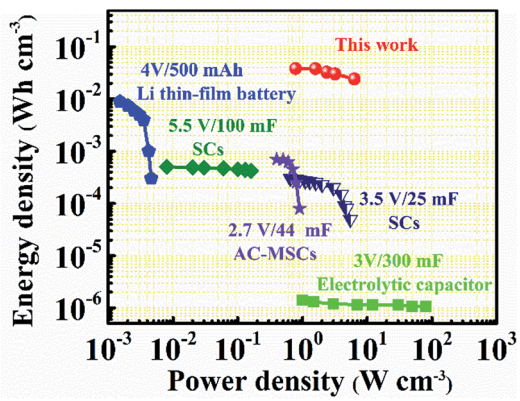

Fig. 5 Ragone plot of all-solid-state PNG//PNG–MoO_2-AMSCs and commercially available energy storage devices.

a power density of 0.8 W cm^{-3} (areal energy density of 8.38 mW h cm^{-2} at 174.4 mW cm^{-2}), which is much higher than that of commercial Li thin-film batteries (≤10 mW h cm^{-3}), commercial supercapacitors (5.5 V/100 mF, 2.7 V/24 mF and 3.5 V/25 mF), and Al electrolytic capacitors.[65] In addition, such superior volumetric energy density of PNG//PNG–MoO_2-AMSC devices is also better than that of most reported high-power MSCs so far (Table S1†), *e.g.*, photochemically reduced graphene (1.5 mW h cm^{-3}),[56] Sulfur-Doped Graphene (3.1 mW h cm^{-3}),[57] MXenes (18 mW h cm^{-3}),[66] EGMX (1.4 mW h cm^{-3}),[67] LIG–FeOOH//LIG–MnO_2 (2.4 mW h cm^{-3}),[60] MnO_2–PPy//V_2O_5–PANI (19.8 mW h cm^{-3}),[38] VN//$Co(OH)_2$ (12.4 mW h cm^{-3})[43] and RGO//RGO–MoO_2 (5.46 mW h cm^{-3}). Furthermore, our PNG//PNG–MoO_2-AMSCs can reach a maximum power density of 6.4 W cm^{-3} (1370.8 mW cm^{-2}).

Conclusions

In summary, we develop a plasma strategy to obtain nitrogen-doped reduced graphene oxide and ultra-fine MoO_2 for all-solid-state PNG//PNG–MoO_2-AMSCs with diversified planar geometries, high energy density and excellent flexibility. The fabricated devices can be operated at a high working voltage of 1.4 V and deliver a remarkable volumetric capacitance of 152.9 F cm^{-3} and energy density of 38.1 mW h cm^{-3}. More notably, the microdevice exhibits long cycle life, exceptional mechanical stability, and compatibility for various substrates, offering great feasibility to integrate into miniaturized devices and extend the usage scenarios. Therefore, our work paves the way for using plasma functioned reduced graphene oxide and its composite films as high capacitance electrodes and mass fabrication of shape-tailored graphene based AMSCs with a combination of high voltage, high energy density, and robust mechanical flexibility to fulfil the requirement of wearable and flexible electronics.

Conflicts of interest

The authors declare no competing financial interest.

Acknowledgements

This work was financially supported by the Australian Research Council Discovery Program (DP190103290) and the Australian Research Council Discovery Early Career Researcher Award scheme (DE150101617 and DE140100716), National Natural Science Foundation of China (Grant 51572259 and 51872283), National Key R&D Program of China (Grant 2016YFB0100100 and 2016YFA0200200), DICP (DICP ZZBS201708), Dalian National Laboratory For Clean Energy (DNL), CAS, DICP&QIBEBT (Grant DICP&QIBEBT UN201702), and DNL Cooperation Fund, CAS (DNL180310 and DNL180308).

Notes and references

1 N. Liu and Y. Gao, *Small*, 2017, **13**, 1701989.
2 Z.-S. Wu, X. Feng and H.-M. Cheng, *Natl. Sci. Rev.*, 2014, **1**, 277–292.
3 N. A. Kyeremateng, T. Brousse and D. Pech, *Nat. Nanotechnol.*, 2017, **12**, 7.
4 S. Zheng, Z.-S. Wu, S. Wang, H. Xiao, F. Zhou, C. Sun, X. Bao and H.-M. Cheng, *Energy Storage Materials*, 2017, **6**, 70–97.
5 M. Beidaghi and Y. Gogotsi, *Energy Environ. Sci.*, 2014, **7**, 867–884.
6 Q. Li and H. Ardebili, *J. Power Sources*, 2016, **303**, 17–21.
7 M. S. K. Mutyala, J. Zhao, J. Li, H. Pan, C. Yuan and X. Li, *J. Power Sources*, 2014, **260**, 43–49.
8 P. Simon and Y. Gogotsi, in *Nanoscience and Technology: A Collection of Reviews from Nature Journals*, World Scientific, 2010, pp. 320–329.
9 D. Yu, K. Goh, H. Wang, L. Wei, W. Jiang, Q. Zhang, L. Dai and Y. Chen, *Nat. Nanotechnol.*, 2014, **9**, 555.
10 G. Zhou, F. Li and H.-M. Cheng, *Energy Environ. Sci.*, 2014, **7**, 1307–1338.
11 P. Das, Q. Fu, X. Bao and Z.-S. Wu, *J. Mater. Chem. A*, 2018, **6**, 21747–21784.
12 Z. Liu, Z. S. Wu, S. Yang, R. Dong, X. Feng and K. Müllen, *Adv. Mater.*, 2016, **28**, 2217–2222.
13 Z. Niu, L. Zhang, L. Liu, B. Zhu, H. Dong and X. Chen, *Adv. Mater.*, 2013, **25**, 4035–4042.
14 M. F. El-Kady and R. B. Kaner, *Nat. Commun.*, 2013, **4**, 1475.
15 W. Gao, N. Singh, L. Song, Z. Liu, A. L. M. Reddy, L. Ci, R. Vajtai, Q. Zhang, B. Wei and P. M. Ajayan, *Nat. Nanotechnol.*, 2011, **6**, 496.
16 W. W. Liu, Y. Q. Feng, X. B. Yan, J. T. Chen and Q. J. Xue, *Adv. Funct. Mater.*, 2013, **23**, 4111–4122.
17 J. Lin, C. Zhang, Z. Yan, Y. Zhu, Z. Peng, R. H. Hauge, D. Natelson and J. M. Tour, *Nano Lett.*, 2012, **13**, 72–78.
18 Z. S. Wu, K. Parvez, S. Li, S. Yang, Z. Liu, S. Liu, X. Feng and K. Müllen, *Adv. Mater.*, 2015, **27**, 4054–4061.
19 H. Xiao, Z.-S. Wu, L. Chen, F. Zhou, S. Zheng, W. Ren, H.-M. Cheng and X. Bao, *ACS Nano*, 2017, **11**, 7284–7292.
20 L. Peng, X. Peng, B. Liu, C. Wu, Y. Xie and G. Yu, *Nano Lett.*, 2013, **13**, 2151–2157.
21 J. Yan, Q. Wang, T. Wei, L. Jiang, M. Zhang, X. Jing and Z. Fan, *ACS Nano*, 2014, **8**, 4720–4729.
22 J. Qin, S. Wang, F. Zhou, P. Das, S. Zheng, C. Sun, X. Bao and Z.-S. Wu, *Energy Storage Materials*, 2019, **18**, 397–404.
23 S. Zheng, W. Lei, J. Qin, Z.-S. Wu, F. Zhou, S. Wang, X. Shi, C. Sun, Y. Chen and X. Bao, *Energy Storage Materials*, 2018, **10**, 24–31.
24 H. Wang, T. Maiyalagan and X. Wang, *ACS Catal.*, 2012, **2**, 781–794.
25 C. Wang, Y. Zhou, L. Sun, Q. Zhao, X. Zhang, P. Wan and J. Qiu, *J. Phys. Chem. C*, 2013, **117**, 14912–14919.
26 P. Ramakrishnan and S. Shanmugam, *ACS Sustainable Chem. Eng.*, 2016, **4**, 2439–2448.
27 H. M. Jeong, J. W. Lee, W. H. Shin, Y. J. Choi, H. J. Shin, J. K. Kang and J. W. Choi, *Nano Lett.*, 2011, **11**, 2472–2477.
28 Z. S. Wu, A. Winter, L. Chen, Y. Sun, A. Turchanin, X. Feng and K. Müllen, *Adv. Mater.*, 2012, **24**, 5130–5135.
29 Q. Jiang, N. Kurra, M. Alhabeb, Y. Gogotsi and H. N. Alshareef, *Adv. Energy Mater.*, 2018, **8**, 1703043.
30 S. Zhu, L. Li, J. Liu, H. Wang, T. Wang, Y. Zhang, L. Zhang, R. S. Ruoff and F. Dong, *ACS Nano*, 2018, **12**, 1033–1042.
31 P. Yang, Y. Ding, Z. Lin, Z. Chen, Y. Li, P. Qiang, M. Ebrahimi, W. Mai, C. P. Wong and Z. L. Wang, *Nano Lett.*, 2014, **14**, 731–736.
32 K. M. Hercule, Q. Wei, A. M. Khan, Y. Zhao, X. Tian and L. Mai, *Nano Lett.*, 2013, **13**, 5685–5691.
33 R. Shi, C. Han, H. Duan, L. Xu, D. Zhou, H. Li, J. Li, F. Kang, B. Li and G. Wang, *Adv. Energy Mater.*, 2018, **8**, 1802088.
34 D. Wei, Y. Liu, Y. Wang, H. Zhang, L. Huang and G. Yu, *Nano Lett.*, 2009, **9**, 1752–1758.
35 D. Deng, X. Pan, L. Yu, Y. Cui, Y. Jiang, J. Qi, W.-X. Li, Q. Fu, X. Ma and Q. Xue, *Chem. Mater.*, 2011, **23**, 1188–1193.
36 H. Zhang, T. Kuila, N. H. Kim, D. S. Yu and J. H. Lee, *Carbon*, 2014, **69**, 66–78.
37 B. Guo, Q. Liu, E. Chen, H. Zhu, L. Fang and J. R. Gong, *Nano Lett.*, 2010, **10**, 4975–4980.
38 C. Shen, X. Wang, S. Li, W. Zhang and F. Kang, *J. Power Sources*, 2013, **234**, 302–309.
39 Y. Yue, Z. Yang, N. Liu, W. Liu, H. Zhang, Y. Ma, C. Yang, J. Su, L. Li and F. Long, *ACS Nano*, 2016, **10**, 11249–11257.
40 T. M. Dinh, F. Mesnilgrente, V. Conédéra, N. A. Kyeremateng and D. Pech, *J. Electrochem. Soc.*, 2015, **162**, A2016–A2020.
41 H. Pang, Y. Zhang, W.-Y. Lai, Z. Hu and W. Huang, *Nano Energy*, 2015, **15**, 303–312.
42 S. Zheng, J. Ma, Z.-S. Wu, F. Zhou, Y. He, F. Kang, H.-M. Cheng and X. Bao, *Energy Environ. Sci.*, 2018, **12**, 1534–1541.
43 S. Wang, Z.-S. Wu, F. Zhou, X. Shi, S. Zheng, J. Qin, H. Xiao, C. Sun and X. Bao, *npj 2D Materials and Applications*, 2018, **2**, 7.
44 W. S. Hummers Jr and R. E. Offeman, *J. Am. Chem. Soc.*, 1958, **80**, 1339.
45 X. Chen, Z. Zhang, X. Li, C. Shi and X. Li, *Chem. Phys. Lett.*, 2006, **418**, 105–108.
46 H. Xiao, Z.-S. Wu, F. Zhou, S. Zheng, D. Sui, Y. Chen and X. Bao, *Energy Storage Materials*, 2018, **13**, 233–240.

47 S. W. Lee, C. Mattevi, M. Chhowalla and R. M. Sankaran, *J. Phys. Chem. Lett.*, 2012, **3**, 772–777.
48 Y. Xue, B. Wu, L. Jiang, Y. Guo, L. Huang, J. Chen, J. Tan, D. Geng, B. Luo and W. Hu, *J. Am. Chem. Soc.*, 2012, **134**, 11060–11063.
49 H. Fei, J. Dong, M. J. Arellano-Jiménez, G. Ye, N. D. Kim, E. L. Samuel, Z. Peng, Z. Zhu, F. Qin and J. Bao, *Nat. Commun.*, 2015, **6**, 8668.
50 T. Lin, I.-W. Chen, F. Liu, C. Yang, H. Bi, F. Xu and F. Huang, *Science*, 2015, **350**, 1508–1513.
51 D. Liu, W. Lei, D. Portehault, S. Qin and Y. Chen, *J. Mater. Chem. A*, 2015, **3**, 1682–1687.
52 Z.-H. Sheng, L. Shao, J.-J. Chen, W.-J. Bao, F.-B. Wang and X.-H. Xia, *ACS Nano*, 2011, **5**, 4350–4358.
53 W. Zhang, C. Xu, C. Ma, G. Li, Y. Wang, K. Zhang, F. Li, C. Liu, H. M. Cheng and Y. Du, *Adv. Mater.*, 2017, **29**, 1701677.
54 M. Yu, X. Cheng, Y. Zeng, Z. Wang, Y. Tong, X. Lu and S. Yang, *Angew. Chem.*, 2016, **128**, 6874–6878.
55 P. Ju, Z. Zhu, X. Shao, S. Wang, C. Zhao, X. Qian and C. Zhao, *J. Mater. Chem. A*, 2017, **5**, 18777–18785.
56 S. Wang, Z.-S. Wu, S. Zheng, F. Zhou, C. Sun, H.-M. Cheng and X. Bao, *ACS Nano*, 2017, **11**, 4283–4291.
57 Z.-S. Wu, Y.-Z. Tan, S. Zheng, S. Wang, K. Parvez, J. Qin, X. Shi, C. Sun, X. Bao and X. Feng, *J. Am. Chem. Soc.*, 2017, **139**, 4506–4512.
58 F. Zhou, H. Huang, C. Xiao, S. Zheng, X. Shi, J. Qin, Q. Fu, X. Bao, X. Feng and K. Müllen, *J. Am. Chem. Soc.*, 2018, **140**, 8198–8205.
59 X. Shi, Z. S. Wu, J. Qin, S. Zheng, S. Wang, F. Zhou, C. Sun and X. Bao, *Adv. Mater.*, 2017, **29**, 1703034.
60 L. Li, J. Zhang, Z. Peng, Y. Li, C. Gao, Y. Ji, R. Ye, N. D. Kim, Q. Zhong and Y. Yang, *Adv. Mater.*, 2016, **28**, 838–845.
61 C. Zhang, J. Xiao, L. Qian, S. Yuan, S. Wang and P. Lei, *J. Mater. Chem. A*, 2016, **4**, 9502–9510.
62 M. Toupin, T. Brousse and D. Bélanger, *Chem. Mater.*, 2002, **14**, 3946–3952.
63 X. Li, J. Shao, J. Li, L. Zhang, Q. Qu and H. Zheng, *J. Power Sources*, 2013, **237**, 80–83.
64 E. Zhou, C. Wang, Q. Zhao, Z. Li, M. Shao, X. Deng, X. Liu and X. Xu, *Ceram. Int.*, 2016, **42**, 2198–2203.
65 D. Pech, M. Brunet, H. Durou, P. Huang, V. Mochalin, Y. Gogotsi, P.-L. Taberna and P. Simon, *Nat. Nanotechnol.*, 2010, **5**, 651.
66 Y.-Y. Peng, B. Akuzum, N. Kurra, M.-Q. Zhao, M. Alhabeb, B. Anasori, E. C. Kumbur, H. N. Alshareef, M.-D. Ger and Y. Gogotsi, *Energy Environ. Sci.*, 2016, **9**, 2847–2854.
67 H. Li, Y. Hou, F. Wang, M. R. Lohe, X. Zhuang, L. Niu and X. Feng, *Adv. Energy Mater.*, 2017, **7**, 1601847.